# Level-crossing induced spin phenomena in SiC: A theoretical study

Denis V. Sosnovsky ⬤ and Konstantin L. Ivanov ⬤ [*]

*International Tomography Center, Siberian Branch of the Russian Academy of Sciences, Novosibirsk 630090, Russia*
*and Novosibirsk State University, Novosibirsk 630090, Russia*

A theoretical approach is proposed to describe the spin dynamics in defect color centers. The method explicitly considers the spin dynamics in the ground state and excited state of the defect center as well as spin state dependent transitions involving the ground state, excited state, and an additional intermediate state. The proposed theory is applied to treat spin-dependent phenomena in silicon carbide, namely, in spin-$\frac{3}{2}$ silicon-vacancy centers, termed $V_{Si}$ or $V2$ centers. Theoretical predictions of magnetic field dependent photoluminescence intensity and optically detected magnetic resonance spectra demonstrate an important role of level-crossing phenomena in the spin dynamics of the ground state and excited state. The results are in good agreement with previously published experimental data [Phys. Rev. X **6**, 031014 (2016)].

## I. INTRODUCTION

Defect color centers are promising objects for various applications, such as optical detection of magnetic resonance [1–3], quantum information processing [4,5], nanosensing [6–11], and nuclear spin hyperpolarization [12–17]. An example of a particularly well studied and widely used system of this kind is given by the negatively charged nitrogen-vacancy centers, $NV^-$ centers, in diamond crystals [1,2]. However, defect color centers in other crystal systems also hold a great promise for similar applications, notably, defect centers in silicon carbide (SiC) and boron nitride [18]. Previous investigations on such colors centers were very often performed by means of optically detected magnetic resonance (ODMR) experiments, which are based on optical initialization and read out of a spin state, which can be manipulated by a resonant radio-frequency (rf) field. Alternatively, the intensity of photoluminescence emitted by a quantum center can also vary without oscillating magnetic field, by sweeping the static external magnetic field. The latter effect is based on level-crossing phenomena and can be used to probe the nanoscale environment.

This work is focused on spin phenomena in 4*H*-SiC [19], specifically, we study silicon-vacancy centers, $V_{Si}$ or $V2$ centers [11,20–23]. These are negatively charged paramagnetic spin-$\frac{3}{2}$ defect states. One should note that there is still a debate on the microscopic structure of the $V_{Si}$ defect. According to electron-nuclear double resonance experiments, authors of Ref. [24] have proposed a model of negatively charged silicon vacancies noncovalently bonded to diamagnetic neutral carbon vacancies located at the adjacent site along the SiC *c* axis. However, presently a majority of the community accepts the model of the isolated $V_{Si}$ defect [25]. Defect centers in SiC are promising candidates for various applications [26–32],

including coherent control of optically addressable spin qubits at room temperature, magnetometry, and thermometry. The aim of this work is to develop a theoretical framework for describing spin phenomena in such a system, notably, phenomena originating from spin mixing at level crossings. The complexity of the problem under study comes from two factors: (i) interplay between the spin dynamics in the excited and ground state of the color center; (ii) the presence of high-spin states, specifically, of $S = \frac{3}{2}$ states. To solve this problem, we generalize an approach [33], which we used earlier to describe optically induced spin polarization formed in $NV^-$ centers in diamonds and in triplet states in molecular crystals. In this method, we explicitly treat the spin dynamics in the ground state and excited states; the transitions between the ground and excited states are introduced using the Lindblad formalism [34,35], which can be efficiently exploited to describe relaxation phenomena in color centers [36–38]. To gain insight into the spin dynamics, we also look at level crossings (LCs) of the spin states and determine under what conditions they are turned into level anticrossings (LACs). As discussed previously, LACs give rise to pronounced features in the magnetic field dependence of photoluminescence (PL) of color centers [39–45] and in ODMR spectra [45]. Hence, this work is dedicated to consideration of level-crossing phenomena in SiC. In practice, LCs are rarely met, since any perturbation would turn them into LACs, giving rise to quantum-mechanical mixing of spin states. For this reason, we look at LACs and their manifestation in PL and ODMR. We demonstrate that the proposed theory can be used to model spin-dependent phenomena in defect centers in SiC, giving a good agreement between calculated and experimental [45] ODMR spectra and magnetic field dependent PL intensity. When necessary, one can extend the treatment to consider cross-relaxation phenomena [46,47], which are commonly encountered in $NV^-$ centers [2,3]. In the context of defect color centers, the term "cross relaxation" stands for coherent polarization exchange between two different centers under LAC conditions.

[*]Corresponding author: ivanov@tomo.nsc.ru
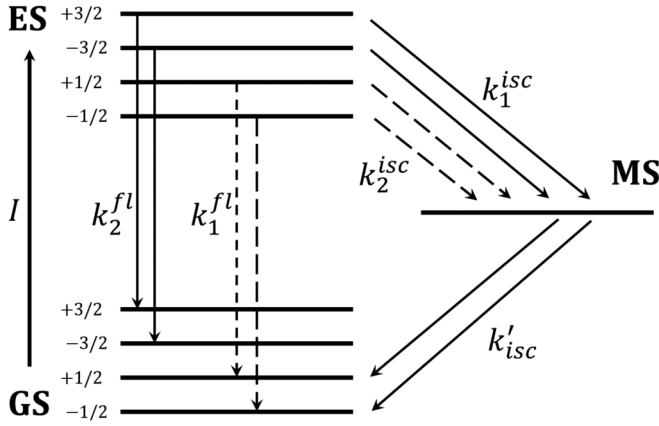
SCHEME 1. Energy level diagram of the silicon-vacancy center in SiC, having the $S = \frac{3}{2}$ electronic ground state and excited state. Transitions between these two states occur at a rate $I$ due to photoexcitation; transitions from the excited state to the ground state are also possible via fluorescence, with the fluorescence rate depending on the spin state of the defect center, i.e., $k_1^{fl} \neq k_2^{fl}$. Transitions to the ground state are also possible via another route: ISC from the excited state to an intermediate state MS with $k_1^{isc} \neq k_2^{isc}$ followed by ISC from this state to the ground state at a rate $k'_{isc}$. Due to the spin-selective character of the transitions, after a few excitation cycles the defect center becomes spin-polarized.

## II. THEORY

Here we consider the energy level diagram of the $V_{Si}$ color center, shown in scheme 1. The system undergoes transitions between the ground state (GS) and excited state (ES) due to light excitation (inducing reversible transitions occurring at a rate $I$); from ES the system goes back to GS via radiative transitions, giving rise to fluorescence. The rate of these transitions depends on the spin state of the defect center, being equal to $k_1^{fl}$ and $k_2^{fl}$ for the $S_z = \pm\frac{1}{2}$ states and $S_z = \pm\frac{3}{2}$ states, respectively. The transition from ES to GS can also take another route: inter-system crossing (ISC) to an intermediate state MS followed by ISC to the ground state. We also assume that the rate of the ISC process from ES to the intermediate state differs for the $S_z = \pm\frac{1}{2}$ states and $S_z = \pm\frac{3}{2}$ states (the corresponding rates are denoted as $k_1^{isc}$ and $k_2^{isc}$, respectively) and that from the intermediate state transitions are possible only to the $S_z = \pm\frac{1}{2}$ spin states in GS (with the rate denoted $k'_{isc}$). These assumptions are consistent with literature data [11,27]; similar relations for rates ($S_z$ dependent fluorescence rates and ISC rates) are known for $NV^-$ centers [2,3]. Due to the difference in the rates, namely $k_1^{fl} \neq k_2^{fl}$, $k_1^{isc} \neq k_2^{isc}$, and $k'_{isc} \neq 0$, only for the $S_z = \pm\frac{1}{2}$ states, after several excitation cycles the $V_{Si}$ defect acquires spin polarization [11,27], that is, the populations of the $S_z = \pm\frac{3}{2}$, $\pm\frac{1}{2}$ states become different in GS and in ES. For the sake of generality, we also assume that the defect center also has a magnetic spin-$\frac{1}{2}$ nucleus coupled to the unpaired electrons.

In principle, the model of the optical excitation cycle might also include spin-dependent $I$ rates, i.e., photoexcitation rates. Furthermore, one might also consider weak transitions from the MS state to the $S_z = \pm\frac{3}{2}$ spin states in GS. Such an extension of the theoretical model presented here is straight-
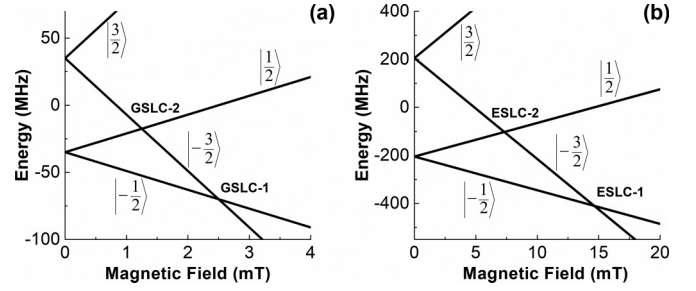
forward. However, with available experimental data we are unable to determine all relevant rates from comparison with experimental data. That is, we cannot discriminate which model is more precise and stick to the model presented in Fig. 1. Calculations performed assuming $k_1^{fl} = k_2^{fl}$, which give similar results, are shown in the Supplemental Material [48] (see, also, Refs. [11,24,33,45,49] therein).

In all cases, we consider the situation where the symmetry axis of the defect center is directed along the $Z$ axis of the lab frame, being parallel (or nearly parallel) to the external magnetic field. As a consequence, the $S_z = \pm\frac{3}{2}$ states and $S_z = \pm\frac{1}{2}$ states are eigenstates of the ES and GS Hamiltonians not only at zero field, but at all magnetic fields, except for the ones corresponding to LACs (see discussion below). At LACs, spin mixing between the $S_z = \pm\frac{3}{2}$ and $S_z = \pm\frac{1}{2}$ states occurs.

For modeling spin-dependent phenomena in $V_{Si}$ centers we use an approach described in our previous paper [33]. First, we introduce the density matrix and Hamiltonian of the defect center in a block-diagonal form:

$$\rho_{SiC} = \begin{pmatrix} \rho_{GS} & 0 & 0 \\ 0 & \rho_{ES} & 0 \\ 0 & 0 & \rho_{MS} \end{pmatrix},$$

$$\hat{\mathcal{H}}_{SiC} = \begin{pmatrix} \hat{\mathcal{H}}_{GS} & 0 & 0 \\ 0 & \hat{\mathcal{H}}_{ES} + \mathcal{E}_{ES}\hat{1} & 0 \\ 0 & 0 & \hat{\mathcal{H}}_{MS} + \mathcal{E}_{MS}\hat{1} \end{pmatrix}. \quad (1)$$

Hence, we introduce both matrices in the basis of spin states $|\mu_{GS}\rangle$, $|\mu_{ES}\rangle$, $|\mu_{MS}\rangle$ defined for each electronic state GS, ES, and MS. If we list these states, the basis becomes $|1_{GS}\rangle, \ldots, |N_{GS}\rangle, |1_{ES}\rangle, \ldots, |N_{ES}\rangle, |1_{MS}\rangle, \ldots, |N'_{MS}\rangle$. Here $N_i$ is the number of spin states in the corresponding state, which is equal to $N$ for GS and ES and to $N'$ for MS ($N' \neq N$ because of the different multiplicity of the electronic states). The form of the density matrix implies that off-diagonal elements of the density matrix can be nonzero for the spin states belonging to the same state GS, ES, or MS, while there are no coherences between the spin states belonging ES, GS, and MS (these matrix elements are subject to very fast decoherence). Hence, for each state (GS, ES, and MS) we introduce its spin density matrix ($\rho_{GS}$, $\rho_{ES}$ and $\rho_{MS}$, respectively). For the sake of simplicity, we also neglect completely the spin dynamics in the MS state. In this situation, we can omit the actual structure of the MS quantum states and set $N' = 2$, corresponding to the two states of the spin-$\frac{1}{2}$ nucleus. This assumption is justified

because in MS there is no LAC-driven spin dynamics (we lump together the electron spin states of MS).

In the Hamiltonian matrix, see Eq. (1), we introduce the energy splitting between GS and ES as $\mathcal{E}_{ES}$, while the energy splitting between GS and MS is denoted as $\mathcal{E}_{MS}$. The spin dynamics in each state is described by the corresponding spin Hamiltonian $\hat{\mathcal{H}}_{GS}$, $\hat{\mathcal{H}}_{ES}$, and $\hat{\mathcal{H}}_{MS}$; here, $\hat{1}$ is the unity matrix of the appropriate dimensionality, i.e., the $N \times N$ or $N' \times N'$ matrix. In the numerical solution procedure, the energies $\mathcal{E}_{ES}$ and $\mathcal{E}_{MS}$ can be omitted (since we are not interested in the coherences between GS, ES, and MS and their evolution).

The density matrices $\rho_{GS}$ and $\rho_{ES}$, see Eq. (1), are introduced in the state basis, which is the direct product of the quartet basis $\mathbb{Q} = \{|\frac{3}{2}\rangle, |\frac{1}{2}\rangle, |-\frac{1}{2}\rangle, |-\frac{3}{2}\rangle\}$ for the electron spin states and the Zeeman basis for the nuclear spin states $\mathbb{Z}$; in the simplest case of a single spin-$\frac{1}{2}$ nucleus $\mathbb{Z} = \{|\frac{1}{2}\rangle, |-\frac{1}{2}\rangle\} = \{|\alpha\rangle, |\beta\rangle\}$ (here $|\alpha\rangle$ and $|\beta\rangle$ are the standard notations for the "spin-up" and "spin-down" states). For $\rho_{MS}$ the basis is introduced as the nuclear Zeeman basis. The spin Hamiltonians describe the Zeeman interaction of spins with the external field **B**, zero-field splitting (ZFS) of the spin-$\frac{3}{2}$ states and electron-nuclear hyperfine coupling (HFC) with the magnetic nucleus of the color center (extension to $K$ magnetic nuclei with arbitrary spin is straightforward). In the case **B**$\|Z$ the Hamiltonians of the quadruplet states are as follows, when written in $\hbar$ units (here we keep in mind that the $E$ parameters in the ZFS tensor are zero, owing to the $C_{3v}$ symmetry of the system):

$$\hat{\mathcal{H}}_{GS} = \gamma_e B \hat{S}_z - \gamma_N B \hat{I}_z + D_G\{\hat{S}_z^2 - \tfrac{5}{4}\} + \mathbf{\hat{S}}\hat{\mathcal{A}}^{(GS)}\mathbf{\hat{I}},$$

$$\hat{\mathcal{H}}_{ES} = \gamma_e B \hat{S}_z - \gamma_N B \hat{I}_z + D_E\{\hat{S}_z^2 - \tfrac{5}{4}\} + \mathbf{\hat{S}}\hat{\mathcal{A}}^{(ES)}\mathbf{\hat{I}}. \quad (2)$$

Here $\mathbf{\hat{S}}$ is the electron spin operator of the spin-$\frac{3}{2}$ state and $\mathbf{\hat{I}}$ is the spin operator of the magnetic nucleus. The first two terms stand for the electron and nuclear Zeeman interactions with $\gamma_e = g_{\|}^{(1)}\mu_B$ and $\gamma_N = g_N\mu_N$ being the corresponding gyromagnetic ratios, where $\mu_B$ and $\mu_N$ stand for the Bohr magneton and nuclear magneton, respectively; $g_{\|}^{(1)}$ and $g_N$ are the corresponding $g$ factors (the subscript $\|$ stands for the $g$ value for the orientation of the defect symmetry axis along the magnetic field). The $D$ terms stand for the ZFS, the last terms stand for HFCs with $\hat{\mathcal{A}}^{(GS/ES)}$ being the HFC tensor in GS and ES. The $D$ parameter for the two GS and ES states in 4$H$-SiC is $D_G = 1.25$ mT and $D_E = 7.32$ mT, respectively [11,22]. The eigenstates of the ZFS Hamiltonian are the $|\frac{3}{2}\rangle, |\frac{1}{2}\rangle, |-\frac{1}{2}\rangle, |-\frac{3}{2}\rangle$ states for both GS and ES. One should also note that the HFC tensors are generally different for the two triplet states, being equal to $\hat{\mathcal{A}}^{(GS)}$ and $\hat{\mathcal{A}}^{(ES)}$. In some cases, we also add various perturbation terms, $\hat{V}_{GS}$ and $\hat{V}_{ES}$, to the GS and ES Hamiltonians:

$$\hat{V}_{GS/ES} = g_{\|}^{(2)}\mu_B \hat{S}_z \left(\hat{S}_z^2 - \frac{5}{4}\right)B + g_{\|}^{(3)}\mu_B \frac{\hat{S}_+^3 - \hat{S}_-^3}{4i}B$$

$$+ g_{\perp}^{(1)}\mu_B \mathbf{\hat{S}}_{\perp}\mathbf{\hat{B}}_{\perp} + g_{\perp}^{(2)}\mu_B \left\{\mathbf{\hat{S}}_{\perp}\mathbf{\hat{B}}_{\perp}, \left(\hat{S}_z^2 - \frac{3}{4}\right)\right\}$$

$$- \frac{i}{4}g_{\perp}^{(3)}\mu_B(\{\hat{S}_+^2, \hat{S}_z\}B_+ - \{\hat{S}_-^2, \hat{S}_z\}B_-). \quad (3)$$

Here $\mathbf{\hat{S}}_{\perp} = (\hat{S}_x, \hat{S}_y)$, $\mathbf{B}_{\perp} = (B_x, B_y)$, $\hat{S}_{\pm} = \hat{S}_x \pm i\hat{S}_y$, $B_{\pm} = B_x \pm iB_y$, $\{\hat{A}, \hat{B}\} = \hat{A}\hat{B} + \hat{B}\hat{A}$ stands for the anticommutator of two operators. The six $g$ factors introduced above are linearly independent in systems of the $C_{3v}$ symmetry [22]. Typically, $g_{\|}^{(1)}$, $g_{\perp}^{(1)} \approx 2$, while the other four $g$ factors are much smaller than unity [11].

The temporal evolution of density matrix of the entire system is described by the Liouville–von Neumann equation

$$\frac{d\rho_{SiC}}{dt} = -i[\hat{\mathcal{H}}_{SiC}, \rho_{SiC}] + \hat{\mathcal{R}}\rho_{SiC} \quad (4)$$

The superoperator $\hat{\mathcal{R}}$ describes the transitions between different states, here GS, ES, and MS, due to light excitation, luminescence, and ISC. It can be written in the Lindblad form, which comprises two terms:

$$\hat{\mathcal{R}}\rho_{SiC} = \{\hat{\mathcal{R}}_1 + \hat{\mathcal{R}}_2\}\rho_{SiC},$$

$$\hat{\mathcal{R}}_1\rho_{SiC} = -\frac{1}{2}\sum_{m,n}\{\hat{\mathcal{L}}_{mn}^{\dagger}\hat{\mathcal{L}}_{mn}\rho_{SiC} + \rho_{SiC}\hat{\mathcal{L}}_{mn}^{\dagger}\hat{\mathcal{L}}_{mn}\},$$

$$\hat{\mathcal{R}}_2\rho_{SiC} = \sum_{m,n}\hat{\mathcal{L}}_{mn}\rho_{SiC}\hat{\mathcal{L}}_{mn}^{\dagger}. \quad (5)$$

The $\hat{\mathcal{R}}_1$ and $\hat{\mathcal{R}}_2$ terms stand for escape from a given state and income to another state, respectively. The operators $\hat{\mathcal{L}}_{mn}$ are defined by introducing the rates $k_{mn}$ of transitions between the quantum states $|m\rangle \to |n\rangle$. They have the following nonzero elements:

$$\langle n|\hat{\mathcal{L}}_{mn}|m\rangle = \sqrt{k_{mn}}. \quad (6)$$

The relevant rates of the processes are indicated in scheme 1. We explain in detail now to introduce the $\hat{\mathcal{L}}_{mn}$ operators in the Supplemental Material.

To calculate the PL intensity, we first evaluate the steady-state value of the density matrix $\rho_{SiC}$. To do so, we solve Eq. (4) setting $\frac{d}{dt}\rho_{SiC} = 0$. To obtain a solution, which is different from the trivial solution $\rho_{SiC} = 0$, we act as follows. Since the rank of the $(-i\hat{\mathcal{H}}_{SiC} + \hat{\mathcal{R}})$ supermatrix is equal to $(M^2 - 1)$ (when $\rho_{SiC}$ is an $M \times M$ matrix), one of the equations in the system $\frac{d}{dt}\rho_{SiC} = 0$ is linearly dependent on the other equations. Therefore, in order to obtain the solution for $\rho_{SiC}$ we replace the last equation in this system by the expression $\sum_i\{\rho_{SiC}\}_{ii} = \text{Tr}\{\rho_{SiC}\} = 1$, which provides normalization of the density matrix. The new system of linear equations is straightforward to solve and $\rho_{SiC}$ can be obtained [33]. Knowing $\rho_{SiC}$, we can compute all experimental observables of interest. For instance, the photoluminescence intensity is given by the following expression:

$$I_{PL} = k_1^{fl}\text{Tr}\{\hat{P}_1^{ES}\rho_{SiC}\} + k_2^{fl}\text{Tr}\{\hat{P}_2^{ES}\rho_{SiC}\}. \quad (7)$$

That is, we multiply the luminescence rate from a specific state by the population of this state. Here $\hat{P}_1^{ES}$ and $\hat{P}_2^{ES}$ are the projector operators onto the $|\pm\frac{1}{2}\rangle$ and $|\pm\frac{3}{2}\rangle$ spin states in ES, respectively. In experiments one can also measure the variation of the PL intensity, applying a weak oscillating magnetic field $\Delta B(t) = \delta B \cos(\omega_{mod}t)$ field along the $Z$ axis and using lock-in detection at the $\omega_{mod}$ frequency. In this case,

instead of the dependence $I_{PL}(B)$ one would measure the field dependence of $\frac{d}{dB}I_{PL}$, i.e., of the derivative of $I_{PL}$.

To calculate the ODMR signal we proceed as follows. First, we add terms describing the interaction with the circularly polarized transverse radio-frequency (rf) field, the $B_1$ field:

$$\hat{\mathcal{H}}_{GS} \rightarrow \hat{\mathcal{H}}_{GS} + \gamma_e B_1 (\cos[\omega_{rf}t]\hat{S}_x + \sin[\omega_{rf}t]\hat{S}_y),$$

$$\hat{\mathcal{H}}_{ES} \rightarrow \hat{\mathcal{H}}_{ES} + \gamma_e B_1 (\cos[\omega_{rf}t]\hat{S}_x + \sin[\omega_{rf}t]\hat{S}_y). \quad (8)$$

Subsequently, we go to the rotating frame, in which the Hamiltonians are written as follows:

$$\hat{\mathcal{H}}'_{GS} = (\gamma_e B - \omega_{rf})\hat{S}_z + \gamma_e B_1 \hat{S}_x - \gamma_N B \hat{I}_z$$
$$+ D_G\left\{\hat{S}_z^2 - \frac{5}{4}\right\} + \hat{\mathbf{S}}\hat{\mathcal{A}}_{sec}^{(GS)}\hat{\mathbf{I}},$$

$$\hat{\mathcal{H}}'_{ES} = (\gamma_e B - \omega_{rf})\hat{S}_z + \gamma_e B_1 \hat{S}_x - \gamma_N B \hat{I}_z$$
$$+ D_E\left\{\hat{S}_z^2 - \frac{5}{4}\right\} + \hat{\mathbf{S}}\hat{\mathcal{A}}_{sec}^{(ES)}\hat{\mathbf{I}}. \quad (9)$$

Here we subtract $\omega_{rf}\hat{S}_z$ from the electronic Zeeman term; in the HFC terms we keep only their secular parts containing the $\hat{S}_z$ operator: the terms containing the $\hat{S}_{x,y}$ operators in the rotating frame are multiplied by fast oscillating exponents $e^{\pm i\omega_{rf}t}$ and can be omitted. It is important to note that transformation to the rotating frame is used only for the electron spins. Using the Hamiltonians from Eq. (9) we calculate the steady-state value of $\rho_{SiC}$ and the PL intensity. The ODMR signal is then proportional to the variation of PL intensity:

$$\text{ODMR} \sim I_{PL}(\text{rf/on}) - I_{PL}(\text{rf/off}), \quad (10)$$

where $I_{PL}(\text{rf/on})$ and $I_{PL}(\text{rf/off})$ is the PL intensity measured in the presence $B_1 \neq 0$ and in the absence $B_1 = 0$ of the rf field. By plotting the ODMR signal as a function of $\omega_{rf}$ we obtain the ODMR spectrum. When the energy separation of the corresponding levels coincides with the frequency of the applied rf field, a spin resonance transition can occur by either absorbing or emitting an rf photon. These rf-induced spin transitions can be detected by monitoring variation of the total PL intensity.

In some cases, for the sake of simplicity, we evaluate the ODMR signal not from Eq. (10); instead we evaluate the difference of the populations $\delta P_{ij}$ of the relevant states $|i\rangle$ and $|j\rangle$ involved in the resonant transition. Assuming that the rf field only slightly perturbs the populations, we calculate the relative ODMR signal, which is given by the intensity ratio $\frac{S_1}{S_2}$, for the transitions $|-\frac{3}{2}\rangle \leftrightarrow |-\frac{1}{2}\rangle$ and $|\frac{3}{2}\rangle \leftrightarrow |\frac{1}{2}\rangle$ in the ground state. In turn, the intensities of these transitions are given by the population differences for the corresponding states:

$$S_1 = \text{Tr}\left\{\hat{P}_{-3/2}^{GS}\rho_{SiC} - \hat{P}_{-1/2}^{GS}\rho_{SiC}\right\},$$

$$S_2 = \text{Tr}\left\{\hat{P}_{3/2}^{GS}\rho_{SiC} - \hat{P}_{1/2}^{GS}\rho_{SiC}\right\}. \quad (11)$$

Here $\hat{P}_{\pm 1/2}^{GS}$ and $\hat{P}_{\pm 3/2}^{GS}$ are the projector operators on the $|\pm\frac{1}{2}\rangle$ and $|\pm\frac{3}{2}\rangle$ ground electronic states, respectively.

Finally, we introduce the typical parameters used in the calculation. The relevant rates, ZFS parameters, and HFC parameters are listed in Table I. For the HFC we assume that the paramagnetic defect center is coupled to a single $^{29}$Si nucleus (spin-$\frac{1}{2}$ nucleus) of the lattice. The HFC tensor is taken symmetric in most cases and the HFC constant is

TABLE I. Parameters of the $V_{Si}$ center used in calculations.

| | |
|---|---|
| Transition rates (ns$^{-1}$) | $I = 0.01$, $k'_{isc} = 0.01$, $k_2^{fl} = 2k_1^{fl} = 0.1$, $k_1^{isc} = 20k_2^{isc} = 0.2$ |
| ZFS parameters (mT) | $D_G = 1.25$, $D_E = 7.32$ |
| HFC tensor of $^{29}$Si (mT) | $A_{xx}^{(GS)} = A_{yy}^{(GS)} = A_{zz}^{(GS)} = 0.001$; $A_{xx}^{(ES)} = A_{yy}^{(ES)} = A_{zz}^{(ES)} = 0.001$ |

taken the same in GS and ES. We would like to note that the HFC is taken small; consequently, the main term causing mixing at LCs (and converting them into LACs) is coming from misalignment of the defect to the external magnetic field. We have done so deliberately in order not to complicate the discussion by interplay of different mechanisms; however, in the Supplemental Material we present the calculation for stronger HFC as well. When necessary, using the same theory, one can also consider HFC with $^{13}$C nuclei, which are, however, not present for most defect centers because of their low natural abundance. Unless otherwise stated, we use the parameters from Table I; when this is not the case, we add a clarifying note. The ZFS parameters have been determined in previous works, while the rates follow from fitting experimental data, presented in Sec. III. The $D_G$ and $D_E$ values are positive, in accordance with previous work [11]. As discussed in the Supplemental Material, variation of the $D_G$ and $D_E$ sign gives rise to characteristic changes in PL and ODMR, which are not consistent with experiments. The transition rates were chosen to give the best agreement with the experimental data. We do not want to put a strong emphasis on the rates determined from fitting, since multiparametric fits are often not sufficiently accurate. Moreover, the goal of this work is developing a consistent theory to treat the LAC-driven spin dynamics and its interplay with transitions between different spin states, whereas the transition rates should ideally be determined from independent measurements. It is important to note that for different relation between the rates $k_1^{fl}$ and $k_2^{fl}$ and also $k_1^{isc}$ and $k_2^{isc}$ the field dependence of the PL intensity and the shape of the ODMR spectrum vary substantially: LAC-derived features come up as peaks or dips, depending on the precise values of the rates. The parameters given in Table I provide the proper appearance of all these features, which is consistent with available experimental data [45]. The rates that we use are in reasonable agreement with previously reported values [49]. In the Supplemental Material we provide additional comments on the choice of the relevant parameters.

## III. RESULTS AND DISCUSSION

### A. LAC analysis

To gain understanding of the spin phenomena, it is useful to support numerical calculations by the analysis of level crossings. When the defect center is oriented nearly parallel (a small misalignment of the two axes is taken into account) to the external field, there are LCs in both GS and ES, occurring at well-defined magnetic fields; see Fig. 1. In each case, there are two LCs, which we name GSLCs and ESLCs. Additional terms would turn these LCs into LACs, as discussed below.

To obtain the LC field positions, we proceed as follows. We omit all terms in the Hamiltonian, except for the electron Zeeman interaction and ZFS interaction. In this situation, the eigenproblem of the Hamiltonian can be solved analytically; at all fields the eigenstates are the states with a specific $S_z$ value, which is $\pm\frac{1}{2}$ or $\pm\frac{3}{2}$. From the solution, one can obtain [22] that at $D > 0$ there is a crossing between the levels corresponding to the $|-\frac{3}{2}\rangle$ and $|-\frac{1}{2}\rangle$ states, which occurs when $\omega_e = \gamma_e B = 2D$ ($\Delta S_z = 1$, hereafter LC-1), and to the $|-\frac{3}{2}\rangle$ and $|\frac{1}{2}\rangle$ states, which occurs when $\omega_e = \gamma_e B = D$ ($\Delta S_z = 2$, hereafter LC-2). In the case under study, we obtain four LC positions, see Fig. 1, corresponding to GSLC-1 at $B = 2D_G/\gamma_e \approx 2.5$ mT, GSLC-2 at $B = D_G/\gamma_e \approx 1.25$ mT [see Fig. 1(a)], to ESLC-1 at $B = 2D_E/\gamma_e \approx 14.64$ mT, and to ESLC-2 at $B = D_E/\gamma_e \approx 7.32$ mT [see Fig. 1(b)]. If we introduce HFC with the spin-$\frac{1}{2}$ magnetic nucleus, each LC of the electron spin states will split into four LCs, corresponding to different nuclear spin states. In the main paper, we consider only the case of small HFC, so that this splitting (which is not observed in any of the experiments reported up to date) is negligibly small.

Various perturbations cause mixing of states and turn the LCs discussed above into LACs: the crossings are avoided due to the presence of the perturbation terms, which mix the states. The minimal splitting of the states at the LAC is equal to $2|V_{mn}|$, where $V_{mn} = \langle m|\hat{V}|n\rangle$ is the corresponding matrix element of $\hat{V}$ between the unperturbed states $|m\rangle$ and $|n\rangle$. The perturbation term becomes relevant when $V_{mn}$ is greater than or comparable to the splitting $\delta\mathcal{E}_{mn}$ between the unperturbed energy levels: this condition defines the width of the LAC region. What is important in the context of the present work, at the LAC the states $|m\rangle$ and $|n\rangle$ are no longer the eigenstates of the Hamiltonian. As a consequence, their populations become mixed. In the case of the $V_{Si}$ center, the crossing states are characterized by different $S_z$ values and have different populations due to the properties of the optical cycle of the color center, as discussed in scheme 1. Excitation from the different states also gives rise to different PL intensity. Upon spin mixing at LACs, the populations are redistributed giving rise increase or reduction of the PL intensity. Hence, LACs are expected to give rise to features, such as peaks or dips, in the $I_{PL}(B)$ curve, as shown below.

A detailed analysis of the role of different perturbations, which turn LCs into LACs, is presented in the Supplemental Material. In this analysis, we calculate the relevant $V_{mn}$ matrix elements for different perturbation terms and compare the results of the LAC analysis with numerical results.

Below we consider in detail a single case, which is relevant for the $V_{Si}$ centers. Let us assume that the $Z$ axis of the ZFS tensor is not perfectly aligned along the external magnetic field. In this case, a perturbation term emerges, which can turn LCs into LACs. The perturbation term can be written as follows:

$$\hat{V}_\perp^{(1)} = \gamma_e B \theta \hat{S}_x \qquad (12)$$

Here $\theta$ is the angle between the $Z$ axis of the ZFS tensor and the external magnetic field (we assume that the **B** vector lies in the $XZ$ plane); this angle is taken small, hence $\sin\theta \approx \theta$. One should note that the full Zeeman Hamiltonian comprises

additional terms [11]

$$\hat{V}_\parallel^{(2)} = g_\parallel^{(2)} \mu_B \hat{S}_z \left(\hat{S}_z^2 - \tfrac{5}{4}\right) B \quad \text{and}$$

$$\hat{V}_\perp^{(2)} = g_\perp^{(2)} \mu_B B \theta \{\hat{S}_x, (\hat{S}_z^2 - \tfrac{3}{4})\},$$

which emerge due to nonequivalence of the $Z$ axis and the perpendicular $X, Y$ axes, and terms

$$\hat{V}_\parallel^{(3)} = g_\parallel^{(3)} \mu_B \frac{\hat{S}_+^3 - \hat{S}_-^3}{4i} B \quad \text{and}$$

$$\hat{V}_\perp^{(3)} = -\frac{i}{4} g_\perp^{(3)} \mu_B B \theta \{(\hat{S}_+^2 - \hat{S}_-^2), \hat{S}_z\},$$

which are coming from the trigonal pyramid symmetry of the defect center. The term $\hat{V}_\parallel^{(2)}$ does not cause any mixing of the electronic spin states, moreover $g_\parallel^{(2)} \approx 0$. The term $\hat{V}_\parallel^{(3)}$ causes mixing of only the states $|\frac{3}{2}\rangle$ and $|-\frac{3}{2}\rangle$ and due to the small value of $g_\parallel^{(3)}$ (see the Supplemental Material) slightly shifts the position of the relevant LCs. We neglect this term for the sake of simplicity. The term $\hat{V}_\perp^{(2)}$ gives rise to the same effect as the perturbation $\hat{V}_\perp^{(1)}$. However, because of the small value of $g_\perp^{(2)}$ (see the Supplemental Material), the corresponding matrix element is negligible. The term $\hat{V}_\perp^{(3)}$ is small but nevertheless gives rise to the spin mixing in the first-order perturbation theory, between the states $|-\frac{3}{2}\rangle$ and $|\frac{1}{2}\rangle$. In the calculation $g_\perp^{(3)}$ is taken equal to 0.2 (as explained in the Supplemental Material). Hence, the misalignment term is given by $\hat{V}_\perp = \hat{V}_\perp^{(1)} + \hat{V}_\perp^{(2)} + \hat{V}_\perp^{(3)}$. The perturbation terms $\hat{V}_\perp^{(1)}$ and $\hat{V}_\perp^{(2)}$ cause mixing between the states $|-\frac{3}{2}\rangle$ and $|-\frac{1}{2}\rangle$ (GSLAC-1 and ESLAC-1), whereas the $\hat{V}_\perp^{(3)}$ term mixes the states $|-\frac{3}{2}\rangle$ and $|\frac{1}{2}\rangle$ (GSLAC-2 and ESLAC-2). The mixing matrix elements calculated in the first-order perturbation theory are equal to

$$\left\langle -\frac{3}{2}\left|\hat{V}_\perp^{(1)}\right|-\frac{1}{2}\right\rangle \approx \sqrt{3}D\theta,$$

$$\left\langle -\frac{3}{2}\left|\hat{V}_\perp^{(2)}\right|-\frac{1}{2}\right\rangle \approx \sqrt{3}\kappa D\theta, \qquad (13)$$

$$\langle -3/2|\hat{V}_\perp^{(3)}|-1/2\rangle \approx -i\sqrt{3}\delta D\theta.$$

Here $\kappa = \frac{g_\perp^{(2)}}{g_\parallel^{(1)}}$ and $\delta = \frac{g_\perp^{(3)}}{g_\parallel^{(1)}}$. These perturbations turn the GSLC-1,2 and ESLC-1,2 into the GSLAC-1,2 and ESLAC-1,2, respectively; see Figs. 2(a) and 2(b). In turn, these LACs give rise to features in the field dependence of the PL intensity; see Fig. 2(c). The discussion of the precise choice of parameters, specifically $g$ factors, is presented in the Supplemental Material; the misalignment angle is always taken $\theta = 5°$.

### B. Comparison with experimental data

In this subsection, we provide a comparison of theoretical results with available experimental data [45] on field-dependent PL and ODMR of the $V_{Si}$ centers.

The PL intensity plotted as a function of the external magnetic field is shown in Fig. 3. To ease comparison with experimental data, we plot not the $I_{PL}(B)$ function, as shown in Fig. 2, but the derivative $\frac{d}{dB}I_{PL}$. Under such conditions, each peak or dip in the field dependence is turned into a sharp
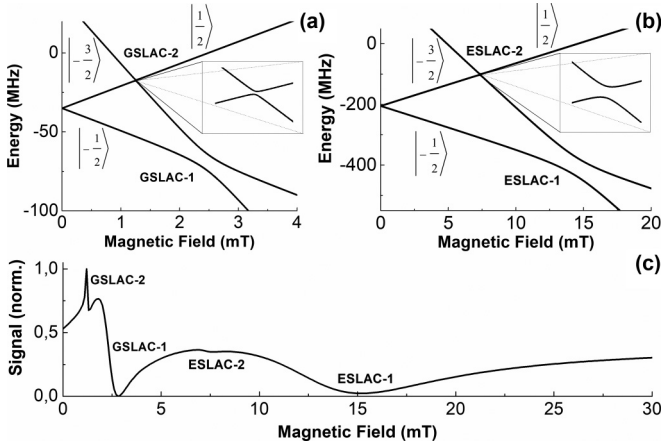
FIG. 2. GSLACs (subplot a) and ESLACs (subplot b) in the $V_{\text{Si}}$ center. The LCs at $\gamma_e B = D_{E,G}$ and $\gamma_e B = 2D_{E,G}$ are turned into LACs by perturbation terms, in this example, by $\hat{V}_\perp = g_\perp^{(1)} \mu_B \hat{\mathbf{S}}_\perp \hat{\mathbf{B}}_\perp + g_\perp^{(2)} \mu_B \{\hat{\mathbf{S}}_\perp \hat{\mathbf{B}}_\perp, (\hat{S}_z^2 - \frac{3}{4})\} - \frac{i}{4} g_\perp^{(3)} \mu_B (\{\hat{S}_+^2, \hat{S}_z\}B_+ - \{\hat{S}_-^2, \hat{S}_z\}B_-)$. The LACs give rise to features in the field dependence of photoluminescence $I_{\text{PL}}(B)$, (normalized to 1), see (subplot c).

feature with a positive component and a negative component (positive-negative feature for a peak and negative-positive feature for a dip). In the field dependence, we can clearly identify the lines originating from the GSLAC-1 and GSLAC-2, whereas the lines from the ESLAC-1 and ESLAC-2 are considerably weaker. Specifically, when the derivative $\frac{d}{dB} I_{\text{PL}}$ is plotted instead of $I_{\text{PL}}$, the smooth ESLAC features, in particular, the ESLAC-1 feature, become barely visible. The relative ratio of the GSLAC and ESLAC lines strongly depends on the relative values of the rates introduced in scheme 1. The type of the feature, i.e., peak or dip, depends on the relation between $k_1^{fl}$ and $k_2^{fl}$ and also between $k_1^{\text{isc}}$ and $k_2^{\text{isc}}$ (the features can only show up when $k_1^{fl} \neq k_2^{fl}$ or $k_1^{\text{isc}} \neq k_2^{\text{isc}}$). The calculated field dependence is in good agreement with the experimental
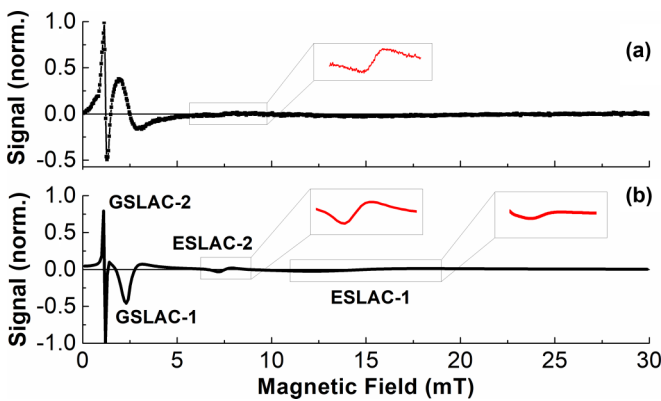


FIG. 3. Photoluminescence intensity $I_{\text{PL}}$ as a function of the static magnetic field $B$, applied nearly parallel to the c-axis of the $V_{\text{Si}}$ center: experimental data (a) and simulation (b). Experimental data were recorded using lock-in detection; in the calculation we show the derivative of $I_{\text{PL}}$, i.e., $\frac{d}{dB} I_{\text{PL}}$, normalized to the maximum value. Features in the field dependence are assigned to the relevant LACs in GS and ES.
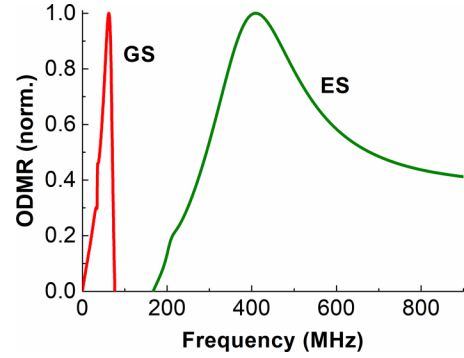


FIG. 4. ODMR spectrum, calculated for zero external magnetic field; the two components correspond to transitions between the ZFS states in GS and ES. The ODMR intensity is normalized to 1 for each transition.

curve: the positions of the features are properly reproduced, as well as their relative intensities and widths.

In addition to the field dependence of PL, we performed calculation of ODMR-related phenomena. First, we consider the case where the external static magnetic field is zero. In this situation, by using the method outlined above, we calculated ODMR spectra, see Fig. 4, with the same parameters as in Fig. 3. In the ODMR spectrum obtained at zero field there are two pronounced features, corresponding to the transitions between the ZFS states with different absolute values of $S_z$, i.e., with $|S_z| = \frac{1}{2}$ and $|S_z| = \frac{3}{2}$. In ES as well as in GS these states are populated differently due to the $S_z$ dependent transitions between GS, ES, and MS. The rf-driven transitions between these states alter the state populations, affecting the PL intensity. In the spectrum, see Fig. 4, we can see two lines at $\omega_{rf}/2\pi \approx 70$ MHz and $\omega_{rf}/2\pi \approx 410$ MHz, corresponding to the rf-driven transitions between the ZFS states in GS and ES, respectively. The feature at 70 MHz is significantly narrower than that at 410 MHz. Such an appearance of the ODMR spectrum is in accordance with experimental spectra [45], which are not shown here.

Second, we calculated the ODMR spectrum under the conditions where $\omega_{rf}$ is fixed, but the magnetic field is swept. The ODMR spectrum is then given by the relative change of PL intensity obtained upon application of the external rf field, which is plotted against the magnetic field strength $B$. An experimental curve is shown in Fig. 5(a) and the calculated dependence is presented in Fig. 5(b). In the simulation, four features emerge, which correspond to the four relevant LACs, GSLAC-1,2 and ESLAC-1,2. Two features are narrow, namely, GSLAC-2 and ESLAC-2, and two features are broad, namely, GSLAC-1 and ESLAC-1. The calculated curve is in good agreement with experimental data [45]. In experimental and theoretical ODMR spectra one can clearly see the features originating from GSLAC-1 and ESLAC-1 (the former is narrower and the latter is broader), while the features associated with GSLAC-2 and ESLAC-2 are barely visible.

## IV. SUMMARY AND CONCLUSIONS

In this work, we present a theoretical formalism, which is capable of describing spin-dependent phenomena related to
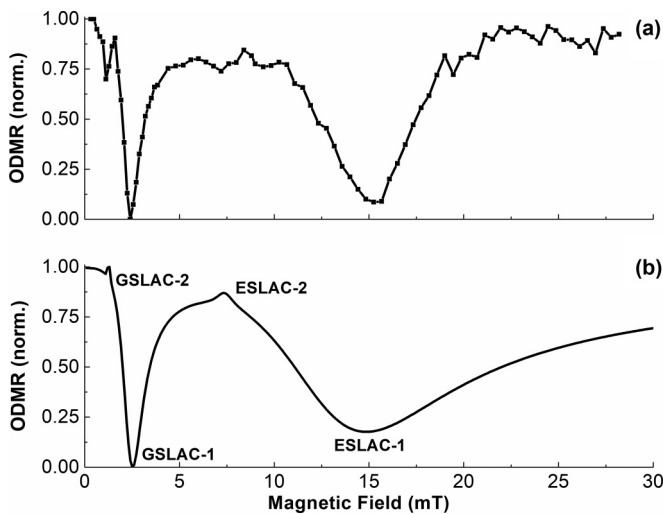
FIG. 5. Normalized relative ODMR signal as a function of the static magnetic field B applied nearly parallel to the c axis of the $V_{Si}$ center: experimental data (a) and simulation (b). Features in the field dependence are assigned to the relevant LACs in GS and ES.

color centers in 4*H*-SiC. Here we focus on the silicon-vacancy centers, $V_{Si}$ or $V2$ centers, having spin-$\frac{3}{2}$ ground state and excited state, which can be polarized by light excitation. Our theoretical method explicitly treats the spin dynamics in both states as well as spin-dependent transitions between the GS, ES, and MS states: this is done by using Lindblad-type superoperators. We demonstrate that the proposed approach can be used to simulate a number of spin-dependent phenomena, namely, magnetic field dependent PL intensity and ODMR

signals, i.e., radio-frequency driven PL changes. Particular focus was put on spin level mixing, which is highly sensitive to external magnetic field and temperature. In the field dependence of the PL intensity sharp peaks and dips are present, which can be assigned to level anticrossing phenomena in ES and GS. We calculate zero-field ODMR spectra obtained by sweeping the frequency of the applied rf field and also the relative changes in the PL intensity, obtained upon variation of the external static magnetic field. In the latter case, features associated with the GSLACs and ESLACs become visible again. Theoretical results are in good agreement with previously reported experimental data [45]. The precise shape of LAC-derived features as well as their phase (peak or dip) were found to depend on the individual rates of the transitions between GS, ES, and MS. The fitting parameters obtained are physically reasonable; nonetheless, for determining them precisely it is desirable to have more experimental data for comparison.

We anticipate that the proposed method can be utilized to describe spin-dependent phenomena in other defect color centers having high spin state. One more application of the present theoretical approach is the analysis of light-induced nuclear spin polarization: such polarization can be observed, for instance, in diamond crystals containing $NV^-$ centers and utilized for dramatic enhancement of weak NMR signals [12–17].

[1] M. W. Doherty, N. B. Manson, P. Delaney, F. Jelezko, J. Wrachtrup, and L. C. L. Hollenberg, Phys. Rep. **528**, 1 (2013).

[2] D. Suter and F. Jelezko, Prog. Nucl. Magn. Reson. Spectrosc. **98-99**, 50 (2017).

[3] D. Suter, Magn. Reson. **1**, 115 (2020).

[4] M. V. Dutt, L. Childress, L. Jiang, E. Togan, J. Maze, F. Jelezko, A. S. Zibrov, P. R. Hemmer, and M. D. Lukin, Science **316**, 1312 (2007).

[5] P. Neumann, N. Mizuochi, F. Rempp, P. Hemmer, H. Watanabe, S. Yamasaki, V. Jacques, T. Gaebel, F. Jelezko, and J. Wrachtrup, Science **320**, 1326 (2008).

[6] J. M. Taylor, P. Cappellaro, L. Childress, L. Jiang, D. Budker, P. R. Hemmer, A. Yacoby, R. Walsworth, and M. D. Lukin, Nat. Phys. **4**, 810 (2008).

[7] B. J. Shields, Q. P. Unterreithmeier, N. P. de Leon, H. Park, and M. D. Lukin, Phys. Rev. Lett. **114**, 136402 (2015).

[8] Y. Wu, F. Jelezko, M. B. Plenio, and T. Weil, Angew. Chem. Int. Ed. **55**, 6586 (2016).

[9] P. Neumann, I. Jakobi, F. Dolde, C. Burk, R. Reuter, G. Waldherr, J. Honert, T. Wolf, A. Brunner, J. H. Shim *et al.*, Nano Lett. **13**, 2738 (2013).

[10] G. Kucsko, P. C. Maurer, N. Y. Yao, M. Kubo, H. J. Noh, P. K. Lo, H. Park, and M. D. Lukin, Nature (London) **500**, 54 (2013).

[11] S. A. Tarasenko, A. V. Poshakinskiy, D. Simin, V. A. Soltamov, E. N. Mokhov, P. G. Baranov, V. Dyakonov, and G. V. Astakhov, Phys. Status Solidi B **255**, 1870101 (2018).

[12] V. Jacques, P. Neumann, J. Beck, M. Markham, D. Twitchen, J. Meijer, F. Kaiser, G. Balasubramanian, F. Jelezko, and J. Wrachtrup, Phys. Rev. Lett. **102**, 057403 (2009).

[13] R. Fischer, C. O. Bretschneider, P. London, D. Budker, D. Gershoni, and L. Frydman, Phys. Rev. Lett. **111**, 057601 (2013).

[14] A. Ajoy, R. Nazaryan, K. Liu, X. Lv, B. Safvati, G. Wang, E. Druga, J. A. Reimer, D. Suter, C. Ramanathan *et al.*, Proc. Natl. Acad. Sci. USA **115**, 10576 (2018).

[15] A. Ajoy, K. Liu, R. Nazaryan, X. Lv, P. R. Zangara, B. Safvati, G. Wang, D. Arnold, G. Li, A. Lin *et al.*, Sci. Adv. **4**, eaar5492 (2018).

[16] P. R. Zangara, S. Dhomkar, A. Ajoy, K. Liu, R. Nazaryan, D. Pagliero, D. Suter, J. A. Reimer, A. Pines, and C. A. Meriles, Proc. Natl. Acad. Sci. USA **116**, 2512 (2019).

[17] V. Ivady, P. V. Klimov, K. C. Miao, A. L. Falk, D. J. Christle, K. Szasz, I. A. Abrikosov, D. D. Awschalom, and A. Gali, Phys. Rev. Lett. **117**, 220503 (2016).

[18] A. Gottscholl, M. Kianinia, V. Soltamov, S. Orlinskii, G. Mamin, C. Bradac, C. Kasper, K. Krambrock, A. Sperlich, M. Toth *et al.*, Nat. Mater. **19**, 540 (2020).

[19] A. L. Falk, B. B. Buckley, G. Calusine, W. F. Koehl, V. V. Dobrovitski, A. Politi, C. A. Zorman, P. X. Feng, and D. D. Awschalom, Nat. Commun. **4**, 1819 (2013).

[20] T. Wimbauer, B. K. Meyer, A. Hofstaetter, A. Scharmann, and H. Overhof, Phys. Rev. B **56**, 7384 (1997).

[21] H. Kraus, V. A. Soltamov, D. Riedel, S. Väth, F. Fuchs, A. Sperlich, P. G. Baranov, V. Dyakonov, and G. V. Astakhov, Nat. Phys. **10**, 157 (2013).

[22] J. Isoya, T. Umeda, N. Mizuochi, N. T. Son, E. Janzén, and T. Ohshima, Phys. Status Solidi B **245**, 1298 (2008).

[23] T. Biktagirov, W. G. Schmidt, U. Gerstmann, B. Yavkin, S. Orlinskii, P. Baranov, V. Dyakonov, and V. Soltamov, Phys. Rev. B **98**, 195204 (2018).

[24] V. A. Soltamov, B. V. Yavkin, D. O. Tolmachev, R. A. Babunts, A. G. Badalyan, V. Yu. Davydov, E. N. Mokhov, I. I. Proskuryakov, S. B. Orlinskii, and P. G. Baranov, Phys. Rev. Lett. **115**, 247602 (2015).

[25] V. Ivády, J. Davidsson, N. T. Son, T. Ohshima, I. A. Abrikosov, and A. Gali, Phys. Rev. B **96**, 161114(R) (2017).

[26] H. Kraus, V. A. Soltamov, F. Fuchs, D. Simin, A. Sperlich, P. G. Baranov, G. V. Astakhov, and V. Dyakonov, Sci. Rep. **4**, 5303 (2015).

[27] Ö. O. Soykal and T. L. Reinecke, Phys. Rev. B **95**, 081405(R) (2017).

[28] D. Simin, F. Fuchs, H. Kraus, A. Sperlich, P. G. Baranov, G. V. Astakhov, and V. Dyakonov, Phys. Rev. Appl. **4**, 014009 (2015).

[29] S.-Y. Lee, M. Niethammer, and J. Wrachtrup, Phys. Rev. B **92**, 115201 (2015).

[30] A. N. Anisimov, D. Simin, V. A. Soltamov, S. P. Lebedev, P. G. Baranov, G. V. Astakhov, and V. Dyakonov, Sci. Rep. **6**, 33301 (2016).

[31] A. L. Falk, P. V. Klimov, B. B. Buckley, V. Ivady, I. A. Abrikosov, G. Calusine, W. F. Koehl, A. Gali, and D. D. Awschalom, Phys. Rev. Lett. **112**, 187601 (2014).

[32] K. Szász, V. Ivády, I. A. Abrikosov, E. Janzén, M. Bockstedte, and A. Gali, Phys. Rev. B **91**, 121201(R) (2015).

[33] D. V. Sosnovsky and K. L. Ivanov, Mol. Phys. **117**, 2740 (2019).

[34] G. Lindblad, Commun. Math. Phys. **48**, 119 (1976).

[35] V. Gorini and A. Kossakowski, J. Math. Phys. **17**, 1298 (1976).

[36] V. Ivády, K. Szász, A. L. Falk, P. V. Klimov, D. J. Christle, E. Janzén, I. A. Abrikosov, D. D. Awschalom, and A. Gali, Phys. Rev. B **92**, 115206 (2015).

[37] K. C. Miao, A. Bourassa, C. P. Anderson, S. J. Whiteley, A. L. Crook, S. L. Bayliss, G. Wolfowicz, G. Thiering, P. Udvarhelyi, V. Ivády *et al.*, Sci. Adv. **5**, eaay0527 (2019).

[38] V. Ivády, Phys. Rev. B **101**, 155203 (2020).

[39] R. Hanson, F. M. Mendoza, R. J. Epstein, and D. D. Awschalom, Phys. Rev. Lett. **97**, 087601 (2006).

[40] R. J. Epstein, F. M. Mendoza, Y. K. Kato, and D. D. Awschalom, Nat. Phys. **1**, 94 (2005).

[41] S. V. Anishchik, V. G. Vins, A. P. Yelisseyev, N. N. Lukzen, N. L. Lavrik, and V. A. Bagryansky, New J. Phys. **17**, 023040 (2015).

[42] A. Wickenbrock, H. Zheng, L. Bougas, N. Leefer, S. Afach, A. Jarmola, V. M. Acosta, and D. Budker, Appl. Phys. Lett. **109**, 053505 (2016).

[43] S. V. Anishchik and K. L. Ivanov, Phys. Rev. B **96**, 115142 (2017).

[44] S. V. Anishchik and K. L. Ivanov, J. Magn. Reson. **305**, 67 (2019).

[45] D. Simin, V. A. Soltamov, A. V. Poshakinskiy, A. N. Anisimov, R. A. Babunts, D. O. Tolmachev, E. N. Mokhov, M. Trupke, S. A. Tarasenko, A. Sperlich *et al.*, Phys. Rev. X **6**, 031014 (2016).

[46] E. van Oort and M. Glasbeek, Phys. Rev. B **40**, 6509 (1989).

[47] R. Akhmedzhanov, L. Gushchin, N. Nizov, V. Nizov, D. Sobgayda, I. Zelensky, and P. Hemmer, Phys. Rev. A **96**, 013806 (2017).

[48] See Supplemental Material at http://link.aps.org/supplemental/10.1103/PhysRevB.103.014403 for expressions for superoperators, LAC analysis, and calculation parameters.

[49] F. Fuchs, B. Stender, M. Trupke, D. Simin, J. Pflaum, V. Dyakonov, and G. V. Astakhov, Nat. Commun. **6**, 7578 (2015).